Comput. Methods Appl. Mech. Engrg. 209–212 (2012) 28–44

Contents lists available at SciVerse ScienceDirect

Comput. Methods Appl. Mech. Engrg.

journal homepage: www.elsevier.com/locate/cma

Topological layout design of electro-fluid-thermal-compliant actuator

Gil Ho Yoon

School of Mechanical Engineering, Hanyang University, Seoul, Republic of Korea

ARTICLE INFO

Article history:
Received 12 October 2010
Received in revised form 26 July 2011
Accepted 4 November 2011
Available online 10 November 2011

Keywords:
Topology optimization
Electro-fluid-thermal-compliant actuator
Multiphysics

ABSTRACT

While the sequential solution procedure (the sequence of solutions) for a steady-state electro-thermal-compliant (ETC) actuator device has been considered in previous studies, very few researches have concurrently considered the mutual couplings between fluid and thermal domains and between fluid and structural domains. Such an analysis allows a straightforward and accurate finite element (FE) simulation of various flow boundary conditions and different flow types, but makes the involved differential equations highly nonlinear. Thus, the goal of this research is to develop a new and rigorous monolithic analysis and optimization framework for an electro-fluid-thermal-compliant (EFTC) microactuator. To accommodate the coupling effect of the fluid and thermal domains, a modified incompressible Navier–Stokes equation with Darcy's force and a heat transfer equation coupled with fluid motion are additionally formulated in the present research. In addition, a new nonlinear monolithic FE modeling method that involves the use of the deformation tensor is employed in order to consider the mutual coupling between fluid and structural domains. Using the solid isotropic material with penalization (SIMP) approach to interpolate seven material properties (Young's modulus, electrical conductivity, heat conductivity, heat capacity, mass density, heat capacity, and Darcy's force coefficient) with respect to a density design variable, it is possible to achieve topology optimization (TO) upon consideration of the strong nonlinear couplings of the EFTC actuator. To efficiently solve four sets of nonlinearly coupled equations, a sequence of iterative solutions to the equations is proposed and a nonlinear sensitivity analysis without consideration of the iterative solution sequence is derived based on the adjoint sensitivity analysis method. Several three-dimensional examples are also examined in order to demonstrate the validity and potential of the present formulations for analysis and TO.

© 2011 Elsevier B.V. All rights reserved.

1. Introduction

Since topology optimization (TO) was introduced to achieve stiffer elastic structure design, it has been applied to a wide range of engineering problems and has become an important engineering tool [1–12]. The method is especially advantageous in the design of micro-electro-mechanical systems (MEMS), the working principle of which is often based on more than two nonlinearly coupled physical parameters [13–18]. Many years of extensive research have been devoted to achieving a transition from the application of TO to classical structural problems to applying TO to the non-structural multiphysics systems of practical devices. Such effort is required to develop precise numerical simulation and optimization schemes for the design of multiphysics systems [1,4–7]. One of the most well-known applications of TO for multiphysics systems may be found in the finite element (FE) analysis and structural optimization of electro-thermal-compliant (ETC) actuators, examples of which are shown in Fig. 1 [2,6,7,18–21]. These microactuators utilize a difference in thermal expansion due to electrically generated heat, i.e., Joule heat. Through the application of an electric potential, Joule heating and the associated increase in temperature inside the actuator induce thermal strain, which in turn actuates the microstructure [7,17–21]. Shown in Fig. 1 are U-beam and V-shaped actuators, two typical ETC actuators usually implemented in MEMS [2,18–21]. Recently, the application of microactuators or grippers exposed to an aqueous environment for cellular grasping were recently researched [22–25]. In [23], an SU-8 micro gripper was developed for manipulating biological samples in solution (static liquid). We believe that these actuators are popular for MEMS applications because they are easy to fabricate and can achieve very large strokes and displacements. While the overwhelming majority of existing ETC actuators have a simple geometry (which is convenient for theoretical modeling), such actuators exhibit sub-optimal performance in terms of actuator displacement and strokes. Thus, there is significant room for structural optimization, which would result in the realization of optimal devices and applications [2,6,7,18–21].

Most structural optimization methods for the ETC microactuators are based on a numerical simulation of the three sets of governing equations: the electro potential equation, heat transfer equation, and linear structural equation. By solving these three

E-mail addresses: gilho.yoon@gmail.com, ghy@hanyang.ac.kr, pilotidea@hotmail.com

0045-7825/$ - see front matter © 2011 Elsevier B.V. All rights reserved.
doi:10.1016/j.cma.2011.11.005

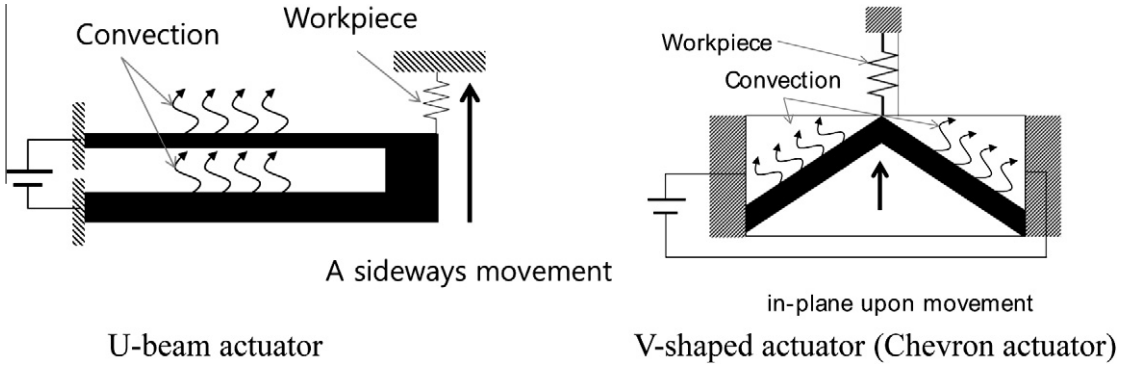

Fig. 1. Conventional MEMS actuators utilizing thermal expansion due to Joule's heat.

coupled equations sequentially, as shown in Fig. 2(a), the performance of the microactuator can be numerically predicted and also can be improved. To the best of our knowledge, relevant research on optimization methods for ETC microactuators is based on several assumptions to simplify the analysis procedure. First, for the sake of simplicity in the numerical analysis and optimization process, the involved materials are often modeled as linear: Improvements in the behavior modeling of nonlinear materials with respect to temperature has been previously reported [7,14]. In the second assumption, thermal boundary conditions such as the convection phenomenon and the conduction, which controls the dissipation of the generated Joule's energy into the fluid surrounding the main device, are simplified that has enjoyed a wide acceptance and works well. Constant surface and side convections are used rather than simulations of sophisticated forced or natural convection, conduction, or radiation phenomena. Although heat dissipation in MEMS devices mainly occurs through conduction as well as convection, complex heat transfer processes can be simplified by constant convection. This assumption has been widely accepted and verified by many researches. Furthermore, some researchers have extended behavior modeling to consider the fluid effect in order to detail thermal modeling [26–28]. In [28], the effect of forced convection on thermal distribution in micro thermal conductivity detectors was studied. Under the third assumption, the influence of fluid and structure interaction (FSI) on the stroke or actuation displacement is ignored [1,29,30]. As a consequence of the above three assumptions, the existing solution method for ETC-based microsystems can efficiently predict the motions of ETC actuators from a not only analysis but also optimization point of view.

In this research, we aim to improve different aspects of the physics modeling of ETC microdevices by concurrently considering the two bidirectional couplings: the couplings between fluid and thermal domains, and those between fluid and structural domains. We first introduce a modified fluid equation, i.e., the Navier–Stokes equation with Darcy's force, which plays an important role in the two bidirectional couplings [1,5]. One of the benefits of solving the modified fluid equation is that it is possible to directly determine the heat transfer or dissipation rate due to fluid motion, i.e., forced convection and conduction. Changing the flow direction or the type of fluid that is used to offset the generated Joule's heat varies the heat dissipation rate along the structure. In other words, the thermal model for the constant surface and side convections can be improved [31]; however, note that the ETC simulation also works well for simulation and optimization. To consider the coupling between fluid and structural domains, the monolithic analysis and optimization method proposed by the author is implemented. It is expected that, depending on the fluid inlet direction, the magnitude of fluid flow, the material properties of the fluid, and the fluid drag force exerted on the structure will influence the actuation of the microactuator. With a low-pressure or low-speed airflow, the fluid drag force acting on the actuator may not be significant. However, if a high-pressure or high-speed fluid flow is applied, consideration of the forces generated by the fluid can improve the accuracy of the prediction. In order to consider the FSI coupling, the monolithic FE modeling formulation using the deformation tensor is implemented. One of the main differences between the present monolithic modeling approach and the previous staggering or monolithic procedures is that a unified analysis domain that exhibits linear elasticity and also follows the Navier–Stokes equations is employed with the FSI coupling boundary conditions. The coupling boundary conditions for the continuities in traction and velocities are treated in a different manner. Detailed descriptions can be found in [1,32]. Consideration of these additional couplings and equations allows for the design of a novel optimal actuator, which is termed an electro-fluid-thermal-compliant (EFTC) actuator, in this study. The mutual couplings among the four sets of differential equations are shown in Fig. 2(b).

This remainder of this paper is organized as follows. In Section 2, the basic equations for the EFTC actuator are described and the proposed algorithm is developed. The interpolation scheme for

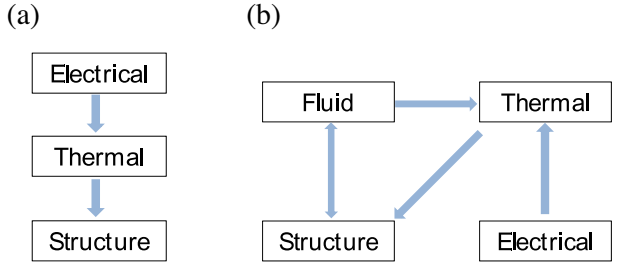

Fig. 2. Comparison between coupling equations of (a) existing electro-thermal-compliant formulation and (b) present electro-fluid-thermal-compliant formulation.

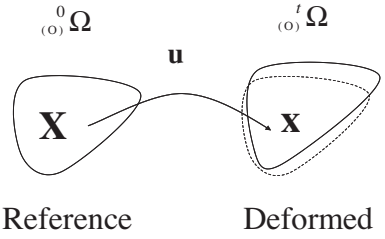

Fig. 3. Reference and deformed configurations.

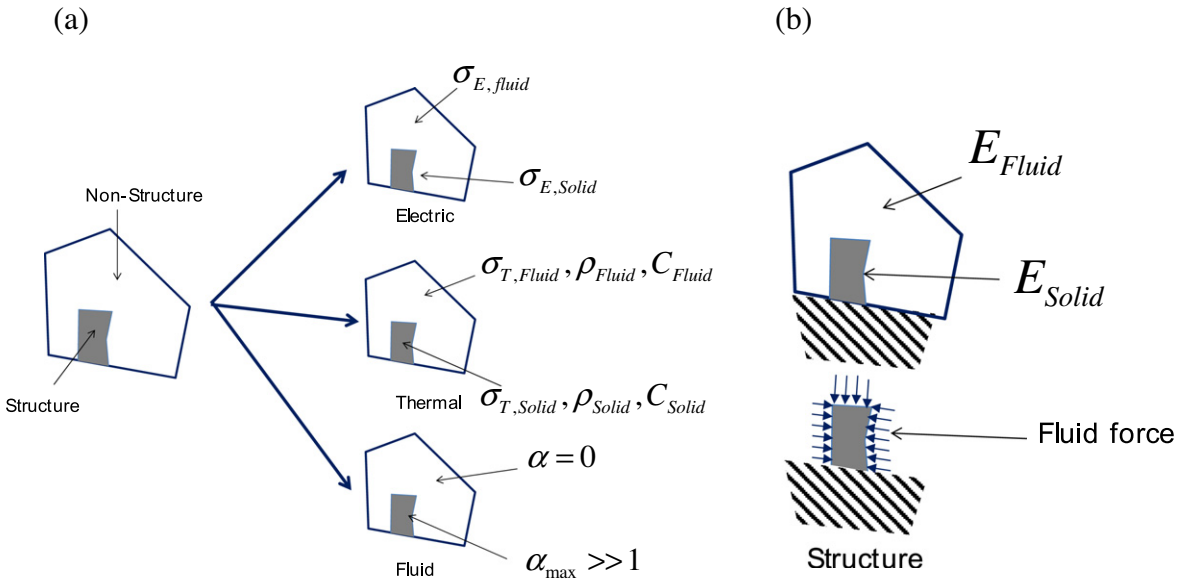

Fig. 4. Domains and material properties of (a) electric, fluid, thermal, and (b) structural domains (electric: the electric conductivities of the solid and fluid are denoted by $\sigma_{E,Solid}$ and $\sigma_{E,fluid}$, respectively. Thermal: the thermal conductivity, capacity, and density of the solid are $\sigma_{T,Solid}$, C_{solid} and ρ_{Solid}, and those of the fluid are $\sigma_{T,Fluid}$,C_{Fluid} and ρ_{Fluid}, respectively. Fluid: the Darcy's force coefficients of the solid and fluid are $\alpha_{\max}$, and 0, respectively. Structure: Young's moduli of the solid and void space are E_{Solid} and E_{Fluid}, respectively).

both the material properties and the physical parameters are also presented. In Section 3, several three-dimensional (3D) numerical examples are considered so as to demonstrate the advantages and disadvantages of the present numerical procedure. Concluding remarks are ultimately presented in Section 4.

2. Unified FE formulation for EFTC system

To derive a unified FE formulation for an EFTC system, four partial differential equations coupled with each other are provided and the development of new numerical procedures for performance and sensitivity analyses is described. In this research, some assumptions are made. First, because the response time of the EFTC microactuator is very short, only the steady-state solution is considered. According to the experiments conducted in [33], it normally takes less than 80 ms to ensure that the assumption of a steady-state solution is feasible. Second, the structural simulations developed here are based on the assumption of small structural displacements; such an assumption results in the spatial differential operators before and after deformation in the parts representing conduction in the electric, thermal, and structure equations being equal [32]. What should be emphasized here is that, due to this assumption, the electric and thermal stiffness matrices become independent of the structural displacements, whereas the force terms of the four systems become dependent on the structural displacements. Furthermore, if the structural displacements become sufficiently large, they should be considered when calculating the stiffness matrices of an EFTC system.

2.1. Monolithic governing equations for EFTC actuator

The EFTC actuator under consideration is characterized by strong mutual couplings even under the assumption that the material is linear. First, the electric potential distribution generates Joule's heat inside the structure. Due to the generated heat, the temperature of the structure increases. The forced convection occurring on the surface of the structure and the conduction through fluid media and anchor cool the structure. According to the experiment and simulation data in [13], heat dissipation through anchor and surrounding fluid is one of key factors in high power consumption. From a structural point of view, both the thermal expansion due to differences in temperature and the surface force due to fluid motion influence the actuation motion of the structure. Furthermore, because the structural displacements

Table 2
Interpolated material properties of present monolithic approach for EFTC device.

		Solid	Fluid
Electric	Conductivity (σ_E)	$\sigma_{E,Solid}$	$\sigma_{E,Fluid}$ ($\ll\sigma_{E,Solid}$)
Fluid	Inverse permeability (α)	$\alpha \gg 0$	0
Thermal	Conductivity (σ_T)	$\sigma_{T,Solid}$	$\sigma_{T,Fluid}$
	Density (ρ)	ρ_{Solid}	ρ_{Fluid}
	Heat capacity (C_p)	C_{Solid}	C_{Fluid}
Linear elasticity	Young's modulus (E)	E_{Solid}	E_{Fluid} ($\ll E_{Solid}$)
	Fluid stress filter (Ψ)	1	0

Table 1
Final equations for electric-fluid-thermal-compliant actuator.

Physics	Weak formulation
Electric potential	$\int_{E^0\Omega} \nabla_{\mathbf{X}}\delta V_E^{\mathrm{T}}\sigma_E\nabla_{\mathbf{X}}V_E\,d\Omega = 0$
Temperature	$-\int_{T^0\Omega} \nabla_{\mathbf{X}}\delta T^{\mathrm{T}}\sigma_T\nabla_{\mathbf{X}}T\,d\Omega = \int_{T^0\Omega}\delta T\left[(\rho C_p\mathbf{v})\nabla_{\mathbf{X}}T - \sigma_E\nabla_{\mathbf{X}}^2V_E\right]d\Omega$
Fluid	$-\int_{F^0\Omega}\delta\mathbf{v}^{\mathrm{T}}\left\{\rho(\mathbf{v}\cdot\mathbf{F}^{-\mathrm{T}}\nabla_{\mathbf{X}}\mathbf{v})\right\}\|\mathbf{F}\|d\Omega = \int_{F^0\Omega}\mathbf{F}^{-\mathrm{T}}\nabla_{\mathbf{X}}\delta\mathbf{v}^{\mathrm{T}}\mathbf{T}_f\|\mathbf{F}\|d\Omega + \int_{F^0\Omega}\alpha\delta\mathbf{v}^{\mathrm{T}}\mathbf{v}\|\mathbf{F}\|d\Omega - \int_{F^0\Gamma_{p^*}}p_{p^*}\mathbf{n}d\Gamma - \int_{F^0\Omega}\delta p^{\mathrm{T}}\{(\nabla_{\mathbf{x}}\cdot\mathbf{v})\}\|\mathbf{F}\|d\Omega = 0$
Structure	$-\int_{S^0\Omega}\delta\mathbf{S}^{\mathrm{T}}\cdot\mathbf{T}_s\,d\Omega = \int_{S^0\Omega}\Psi\cdot\mathbf{F}^{-\mathrm{T}}\delta\mathbf{S}(\mathbf{u},\delta\mathbf{u})^{\mathrm{T}}\cdot p\|\mathbf{F}\|d\Omega + \int_{S^0\Omega}\Psi\cdot\mathbf{F}^{-\mathrm{T}}\delta\mathbf{u}\cdot\nabla_{\mathbf{X}}p\|\mathbf{F}\|d\Omega$

change the fluid domain and the associated fluid–structure interaction boundary condition, some iterative computational procedures among these physics are necessary to produce solutions that consider these mutual and strong couplings. In short, the study of the EFTC nonlinear system is considerably more complicated than that of ETC systems because of the abovementioned couplings.

To provide a rigorous formulation for the EFTC actuator or mechanism, a distinction is made between the coordinates of the undeformed domain, ${}_{(\circ)}{}^{0}\Omega$, and the deformed domain, ${}_{(\circ)}{}^{t}\Omega$, ($\bigcirc = E, F, T, S$ for electric potential, fluid, thermal, and structural domains, respectively) as follows:

$$\mathbf{x} = \mathbf{X} + \mathbf{u}, \tag{1}$$

where $\mathbf{u}$ is the structural displacement and $\mathbf{x} = \{x_i\}$ and $\mathbf{X} = \{X_i\}$ ($i = 1, 2, 3$ for 3D) are the Cartesian coordinates of the material point in the deformed and undeformed domains, respectively (see Fig. 3).

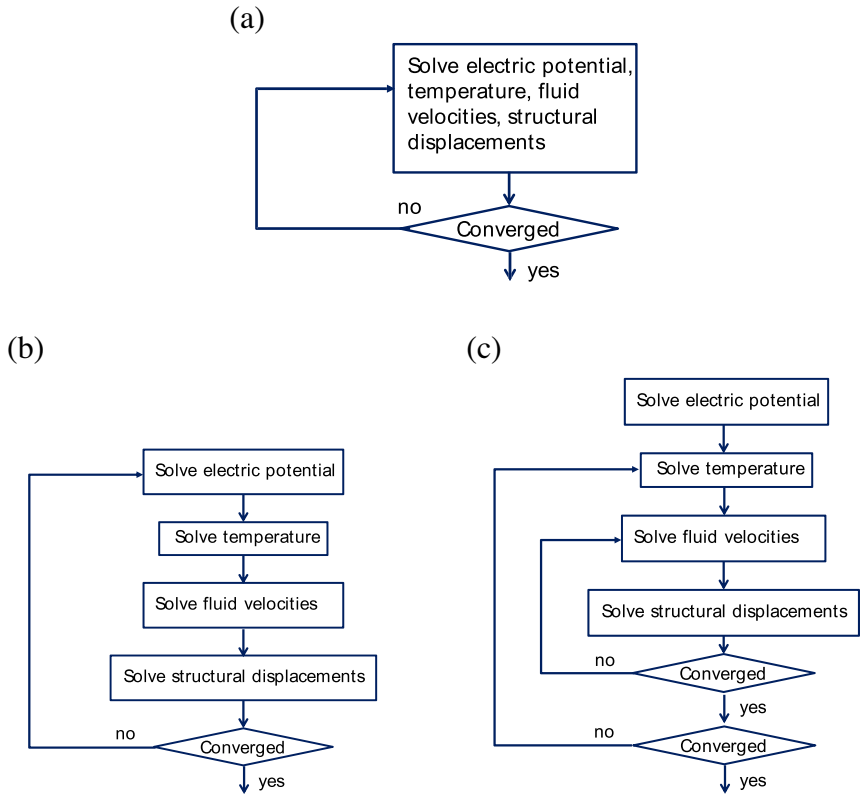

Fig. 5. Solution procedures: (a) monolithic analysis procedure, (b) staggered analysis procedure, and (c) proposed staggered analysis procedure (note that the term "monolithic procedure" is used to indicate the four physics used simultaneously in the analysis and design domains. We distinguish the monolithic design procedure from the monolithic analysis procedure).

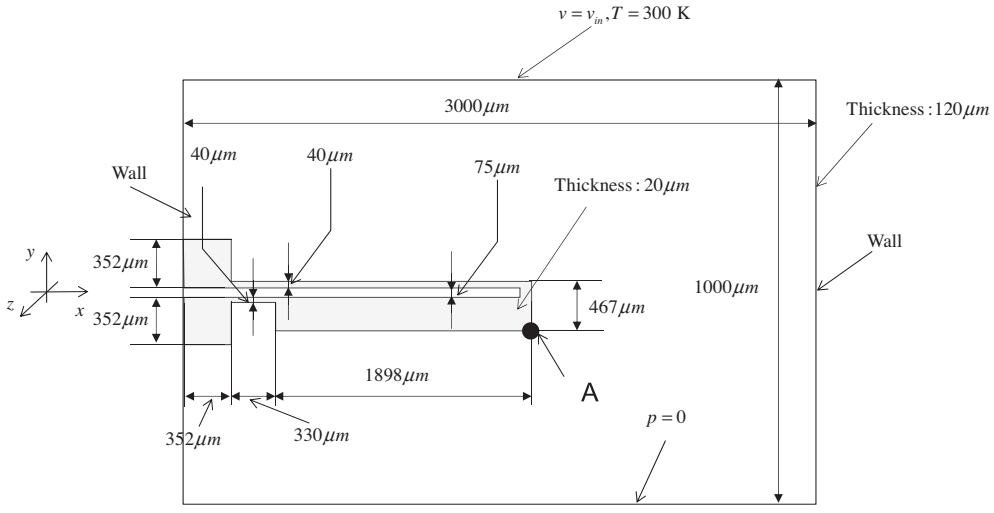

Fig. 6. Analysis example 1 of microactuator (solid: $E = 169$ GPa, $\nu = 0.3$, $\alpha_E = 2.568 \times 10^{-6}$ K^{-1}, $\sigma_T = 146.4$ W/km $\sigma_E = 1/4.2 \times 10^{-4}$ K/Ω m, $\rho = 8908$ kg/m^3, applied voltage = 15 V, bulk temperature = 300 K. Air: $E = 169 \times 10^{-9}$ GPa, $\sigma_T = 0.025$ W/km, $\sigma_E = 10^{-9}/4.2 \times 10^{-4}$ K/Ω m, $\rho = 1.1839$ kg/m^3, $C_{Solid} = 26.07$ J/K,$C_{Fluid} = 1.012$ J/K, viscosity = 17.4 μPa s; Water: electric conductivity = 6.4×10^{-3} K/Ω m, thermal conductivity = 0.6 W/km, specific heat capacity = 4184 J/K, density = 1000 kg/m^3, viscosity = 1.002 mPa s, character length = 120 μm).

This distinction is somewhat necessary in order to consider the abovementioned strong coupling among the four physics.

From the relationship expressed in (1), the deformation tensor **F** (or the deformation gradient) that transforms fundamental quantities such as the mechanical strain, stress, mass density, and volume can be defined. It is well known that this deformation tensor can transform the differential and integral operators of the undeformed and deformed configurations. A thorough analysis of continuum mechanics is given in [1,32]. Using the deformation tensor, the following relationships can be obtained:

$$\mathbf{F} = \frac{\partial \mathbf{x}}{\partial \mathbf{X}}, \tag{2}$$

$$\nabla_{\mathbf{X}} = \mathbf{F}^{\mathrm{T}} \nabla_{\mathbf{x}}, \quad \nabla_{\mathbf{x}} = \mathbf{F}^{-\mathrm{T}} \nabla_{\mathbf{X}} \int_{(\circ)^{t}\Omega} ()\, d\Omega = \int_{(\circ)^{0}\Omega} ()\, \|\mathbf{F}\|\, d\Omega, \tag{3}$$

where $\nabla_{\mathbf{X}}$ and $\nabla_{\mathbf{x}}$ are the differential operators of the undeformed and deformed configurations, respectively. The determinant of the deformation tensor is $\|\mathbf{F}\|$. As stated above, because the configurations of these four domains continuously change during an iterative solution procedure, we emphasize that it is necessary to consider the two coordinates **x** and **X**.

2.1.1. Governing equation for electric potential

Without an internal charge, the electric potential of the structure can be calculated by solving the following Laplace equation:

$$\text{Energy balance}: \quad \nabla_{\mathbf{x}} \cdot (\sigma_E \nabla_{\mathbf{x}} V_E) = 0 \quad \text{in } {}_{E}{}^{t}\Omega(\mathbf{u}), \tag{4}$$

where σ_E is the spatially varying electrical conductivity and V_E is the electric potential. In (4), it should be noted that the differential operator of the deformed domain, ${}_{E}{}^{t}\Omega(\mathbf{u})$, is dependent on the structural displacements (**u**). Therefore, the above equation can be solved iteratively considering the structural displacements. However, in this study, the coupling effect between the differential operator and the structural displacements in the left side of the above equation is neglected. This assumption is similar to the assumption of geometrical linearity in the structural analysis and was verified in

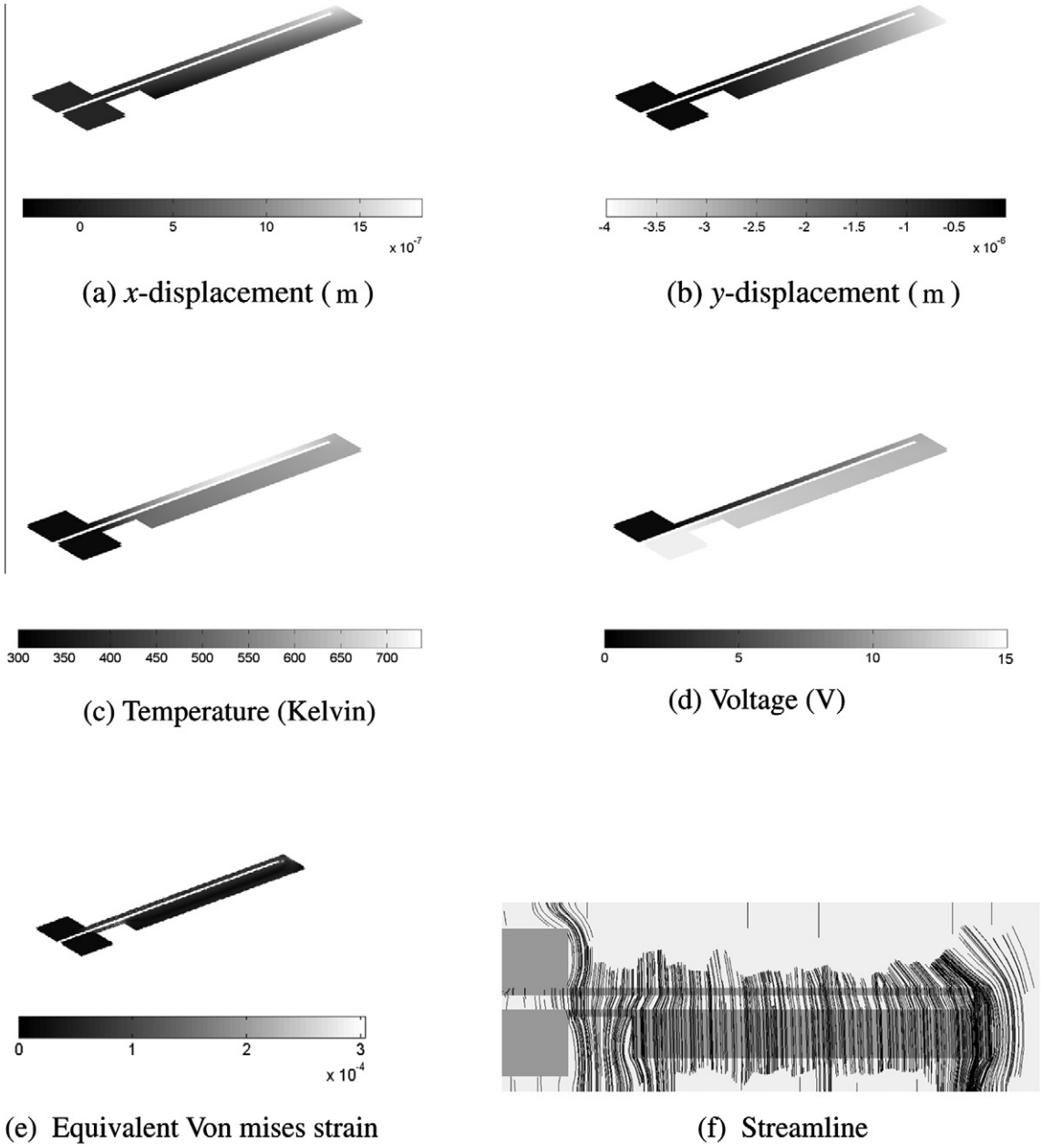

Fig. 7. Structural displacements and fluid (air) motion with fluid velocity of 1 μm/sin$y$-direction.

the electrostatic system in [4]. By neglecting this effect of structural displacements on electric potential, the electric potential can be calculated by solving the following Laplace equation defined at the undeformed domain, ${}_E{}^0\Omega$, in the FE context with appropriate boundary conditions

$$\text{Strong form}: \quad \nabla_{\mathbf{X}} \cdot (\sigma_E \nabla_{\mathbf{X}} V_E) = 0 \quad \text{in } {}_E{}^0\Omega, \tag{5}$$

$$\text{Weak form}: \quad \int_{{}_E{}^0\Omega} \nabla_{\mathbf{X}} \delta V_E^{\mathrm{T}} \sigma_E \nabla_{\mathbf{X}} V_E \, d\Omega = 0 \quad \text{in } {}_E{}^0\Omega, \tag{6}$$

where the virtual electric field is δV_E.

2.1.2. Governing equation for temperature

To calculate the temperature rise in the structure neglecting viscous dissipation and buoyancy, the Joule's heat generation and the heat convection due to fluid motion should be considered as follows:

$$\nabla_{\mathbf{x}} \cdot (\sigma_T \nabla_{\mathbf{x}} T) = (\rho C_p \mathbf{v}) \cdot \nabla_{\mathbf{x}} T - \sigma_E \nabla_{\mathbf{x}}^2 V_E \quad \text{in } {}_T{}^t\Omega(\mathbf{u}), \tag{7}$$

where σ_T, ρ, and C_p are the spatially varying thermal conductivity, density, and heat capacity, respectively. As in Eqs. (4) and (5), we neglect the effect of structural displacements on $\nabla_{\mathbf{x}}$ in Eqs. (5) and (6) and simplify these equations as follows:

$$\text{Strong form}: \quad \nabla_{\mathbf{X}} \cdot (\sigma_T \nabla_{\mathbf{X}} T) = (\rho C_p \mathbf{v}) \cdot \nabla_{\mathbf{X}} T - \sigma_E \nabla_{\mathbf{X}}^2 V_E \quad \text{in } {}_T{}^0\Omega, \tag{8}$$

$$\text{Weak form}: \quad -\int_{{}_T{}^0\Omega} \nabla_{\mathbf{X}} \delta T^{\mathrm{T}} \sigma_T \nabla_{\mathbf{X}} T \, d\Omega = \int_{{}_T{}^0\Omega} \delta T \left[(\rho C_p \mathbf{v}) \nabla_{\mathbf{X}} T - \sigma_E \nabla_{\mathbf{X}}^2 V_E \right] d\Omega \quad \text{in } {}_T{}^0\Omega, \tag{9}$$

where δT is the virtual temperature field.

One of advantages of the above multiphysics modeling is that the assumption of the constant convection for the surface and side convections is not necessary. Because it is usually difficult to model the convection considering fluid motion in MEMS, heuristic or experimental measurements of this phenomenon are often adopted [3,7,8,34]. However, the present theory allows for clear modeling of the convection phenomenon.

2.1.3. Governing equation for fluid: monolithic Navier–Stokes equation

The steady-state Navier–Stokes equation and the incompressibility constraint with the spatial derivative are expressed as follows:

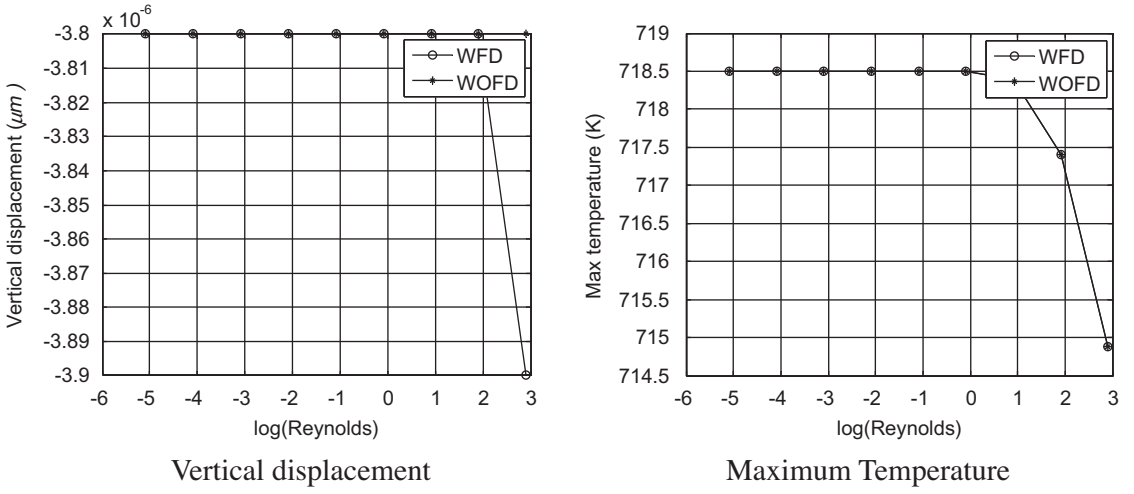

Fig. 8. Numerical tests of the actuator of Fig. 7 with downward fluid flow. Maximum vertical displacement and maximum temperature (a) of air and (b) of water. (WFD: downward fluid with fluid drag force, WOFD: downward fluid without fluid drag force.)

$$\text{Momentum}: \quad \rho(\mathbf{v}\cdot\nabla_{\mathbf{x}})\mathbf{v} = \nabla_{\mathbf{x}}\cdot\mathbf{T}_f - \alpha\mathbf{v} \quad \text{in } {}_F{}^t\Omega(\mathbf{u}), \tag{10}$$

$$\text{Continuity}: \quad -\nabla_{\mathbf{x}}\cdot\mathbf{v} = 0 \quad \text{in } {}_F{}^t\Omega(\mathbf{u}), \tag{11}$$

$$\mathbf{T}_f = -p\mathbf{I} + \mu(\nabla\mathbf{v} + \nabla\mathbf{v}^{\mathrm{T}}), \tag{12}$$

where $\mathbf{v}$ and $\mathbf{T}_f$ are the fluid velocity field and the symmetric stress tensor of incompressible flow, respectively. ρ is the fluid density, which is same as the density in Eq. (9). μ is the constant dynamic viscosity for Newtonian flow. It should be noted that the material derivative operator $\nabla_{\mathbf{x}}$ at time t is also defined for the control volume ${}_F{}^t\Omega(\mathbf{u})$. The steady-state FSI boundary condition (continuity in velocity) is described along the interface boundary ${}_f{}^t\Gamma_i(\mathbf{u}) = {}_s{}^t\Gamma_i(\mathbf{u})$ as follows:

$$\mathbf{v} = \dot{\mathbf{u}} \equiv \mathbf{0} \quad \text{on } {}_f{}^t\Gamma_i(\mathbf{u})(= {}_s{}^t\Gamma_i(\mathbf{u})) \quad \text{(interface boundary condition)}, \tag{13}$$

In Eq. (10), the viscous force, $\alpha\mathbf{v}$, proportional to the fluid velocities is added to the Navier–Stokes equation. This modified Navier–Stokes equation was proposed so as to make it possible to solve the TO problem of the fluid [1,3,5]. In this work, the concept of viscous force for TO of the EFTC device is also adopted. With a sufficiently large value of α, the velocities along the interfacing boundaries approach zero, thus satisfying the condition of the continuity in velocity. As such, a very large value can be assigned to the solid domain for zero fluid velocities inside the structural domain and along the interface boundaries [1,5].

$$\begin{cases} \alpha = \alpha_{\max} \gg 0 & \text{for solid or interface boundaries } (\mathbf{v} \equiv \mathbf{0}), \\ \alpha = 0 & \text{for fluid.} \end{cases} \tag{14}$$

As stated above, the theory of continuum mechanics is used to reformulate (10) and (11) in the undeformed domain, ${}_F{}^0\Omega(\mathbf{u})$:

$$\begin{aligned} &-\int_{{}_F{}^0\Omega} \delta\mathbf{v}^{\mathrm{T}}\{\rho(\mathbf{v}\cdot\mathbf{F}^{-}\mathrm{T}\nabla_{\mathbf{X}}\mathbf{v})\}\|\mathbf{F}\|d\Omega \\ &\quad = \int_{{}_F{}^0\Omega} \mathbf{F}^{-}\mathrm{T}\nabla_{\mathbf{X}}\delta\mathbf{v}^{\mathrm{T}}\mathbf{T}_f\|\mathbf{F}\|d\Omega + \int_{{}_F{}^0\Omega} \alpha\delta\mathbf{v}^{\mathrm{T}}\mathbf{v}\|\mathbf{F}\|d\Omega \\ &\qquad - \int_{{}_F{}^0\Gamma_{p^*}} p_{p^*}\mathbf{n}\,d\Gamma, \end{aligned} \tag{15}$$

$$-\int_{{}_F{}^0\Omega} \delta p^{\mathrm{T}}\{(\nabla_{\mathbf{x}}\cdot\mathbf{v})\}\|\mathbf{F}\|d\Omega = 0, \tag{16}$$

where p_{p^*} is the applied pressure along the boundary ${}_F{}^0\Gamma_{p^*}$ with the normal direction vector $\mathbf{n}$. This transformation of the Navier–Stokes equation between the two configurations using the deformation tensor was originally proposed and validated in our previous work [1].

2.1.4. Governing equation for structure: monolithic linear elasticity equation

In the governing equations for electric, fluid, and temperature domains, the involved material properties of each governing equation are changed for nonstructural and structural domains (see Fig. 4). However, in the linear elasticity equation, explicit boundaries between nonstructural and structural domains are required so as to consider the so-called displacement dependent boundary condition (see [1,2] for details of the displacement dependent boundary condition). In other words, while the concept of employing a sufficiently weak Young's modulus in the right side of (24) can be used to convert the integral of the structural domain to that of the entire domain, the explicit boundary, ${}_s{}^t\Gamma_i(\mathbf{u})\left(= {}_f{}^t\Gamma_i(\mathbf{u})\right)$, which is itself a function of $\mathbf{u}$, should be defined. To address this issue, we define the solid $\left({}_{ms}{}^t\Omega\right)$ and fluid $\left({}_{mf}{}^t\Omega\right)$ domains inside the total analysis domain $\left({}_s{}^t\Omega\right)$ at time t as follows:

$${}_s{}^t\Omega = {}_{ms}{}^t\Omega \cup {}_{mf}{}^t\Omega. \tag{17}$$

Without including the external body force, the governing equation of the structure with thermal expansion can then be formulated with Cauchy's stress, $\mathbf{T}_s$, in the deformed structural domain, ${}_{ms}{}^t\Omega(\mathbf{u})$

$$\mathbf{S} = \frac{1}{2}\left(\nabla_{\mathbf{x}}^{\mathrm{T}}\mathbf{u} + \nabla_{\mathbf{x}}\mathbf{u}\right), \tag{18}$$

$$\mathbf{T}_s = \mathbf{C}(\mathbf{S} - \alpha_E(T - T_0)\mathbf{I}) \quad (\mathbf{I}: \text{Identity tensor}, T_0: \text{ambient temperature}), \tag{19}$$

$$\mathbf{C} = \frac{E(1-\nu)}{(1+\nu)(1-2\nu)} \times \begin{bmatrix} 1 & \frac{\nu}{1-\nu} & & \frac{\nu}{1-\nu} & & \\ \frac{\nu}{1-\nu} & 1 & & \frac{\nu}{1-\nu} & & \\ \frac{\nu}{1-\nu} & \frac{\nu}{1-\nu} & & 1 & & \\ & & \frac{1-2\nu}{2(1-\nu)} & & & \\ & \text{Elements not shown are zeros} & & \frac{1-2\nu}{2(1-\nu)} & & \\ & & & & \frac{1-2\nu}{2(1-\nu)} & \end{bmatrix}, \tag{20}$$

$$\nabla_{\mathbf{x}}\cdot\mathbf{T}_s = 0 \text{ in } {}_{ms}{}^t\Omega(\mathbf{u}) \quad \left({}_{ms}{}^t\Omega(\mathbf{u}): \text{ structural domain}\right), \tag{21}$$

where the linear strain $\mathbf{S}$ and the associated structural stress $\mathbf{T}_s$ are defined above, $\mathbf{C}$ is the linear constitutive matrix, α_E is the thermal expansion coefficient, E is Young's modulus, and ν is Poisson's ratio [32].

For the structural equation, the steady-state fluid–structure interaction boundary condition (continuity in traction) is described as follows:

$$\mathbf{n}\cdot\mathbf{T}_s = \mathbf{n}\cdot\mathbf{T}_f \quad \text{on } {}_s{}^t\Gamma_i(\mathbf{u})(= {}_f{}^t\Gamma_i(\mathbf{u})) \quad \text{(interface boundary condition)}. \tag{22}$$

This condition states that the product of the normal vector and the external fluid stress should be the same as that of the product of the normal vector and the internal mechanical stress along the FSI interaction boundaries. Then, the external work due to the pressure stress tensor ($\mathbf{T}_f$) at the interface boundary condition can be defined as follows:

$$\text{External work} = \int_{{}_s{}^t\Gamma_i} \delta\mathbf{u}^{\mathrm{T}}(\mathbf{n}\cdot\mathbf{T}_f)d\Gamma, \tag{23}$$

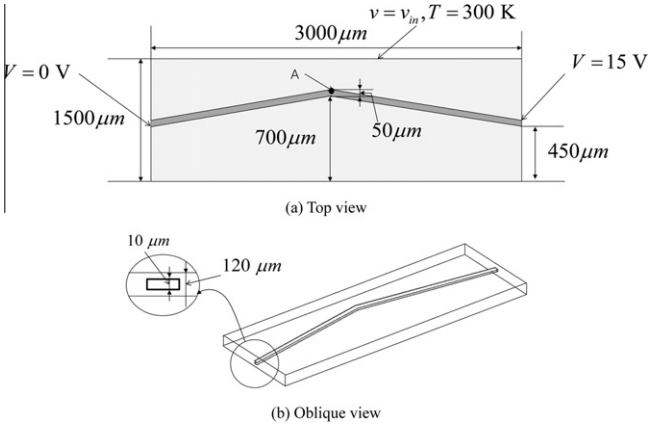

Fig. 9. Analysis example 2 of microactuator (solid: $E = 169$ MPa, $\nu = 0.3$, $\alpha_E = 2.568 \times 10^{-6}$ K^{-1}, $\sigma_T = 146.4$ W/km, $\sigma_E = 1/4.2 \times 10^{-4}$ K/Ω m, $\rho = 8908$ kg/m^3, applied voltage = 15 V, bulk temperature = 300 K. Air: $E = 169 \times 10^{-9}$ GPa, $\sigma_T = 0.025$ W/km, $\sigma_E = 10^{-9}/4.2 \times 10^{-4}$ K/Ω m, $\rho = 1.1839$ kg/m^3, $C_{Solid} = 26.07$ J/K, $C_{Fluid} = 1.012$ J/K, viscosity = 17.4 μPa s. Water: electric conductivity = 6.4×10^{-3} K/Ω m, thermal conductivity = 0.6 W/km, specific heat capacity = 4184 J/K, density = 1000 kg/m^3, viscosity = 1.002 mPa s, character length = 120 μm).

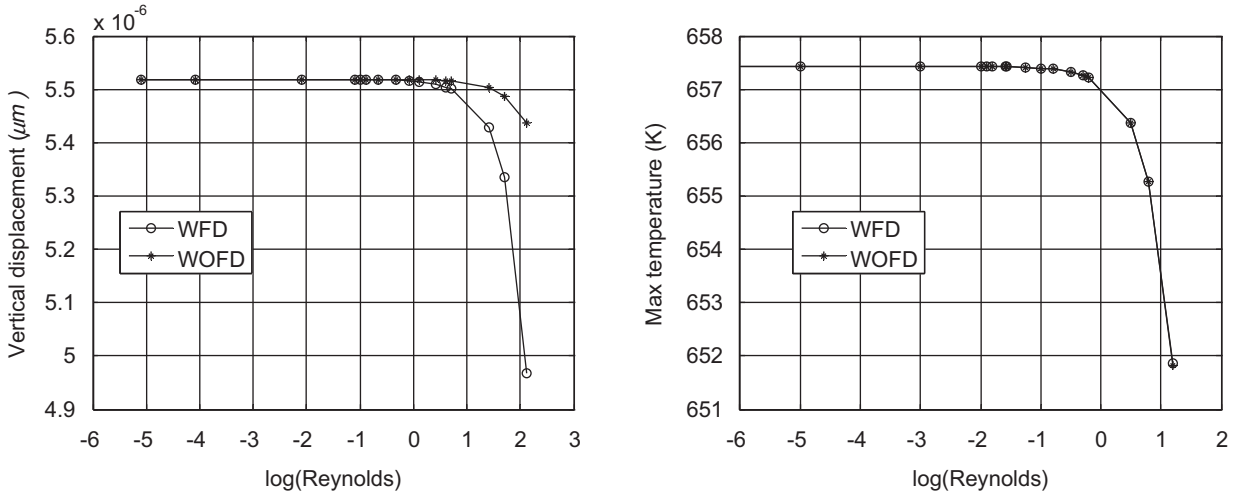

(a) Downward Air Flow

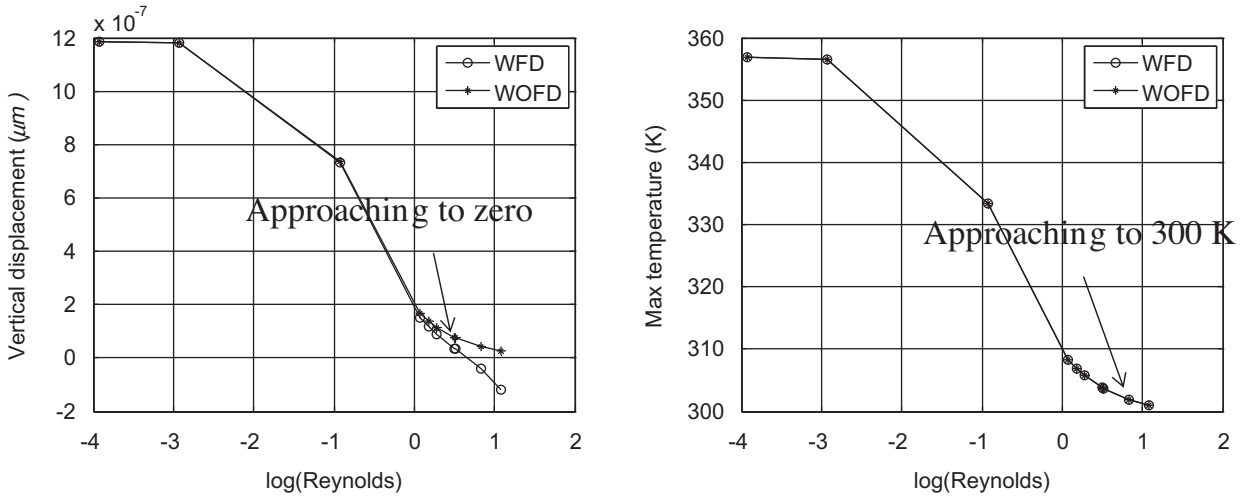

(b) Downward Water Flow

Fig. 10. Numerical tests of the actuator of Fig. 9 with downward flow. Maximum vertical displacement and maximum temperature (a) of air and (b) of water. (WFD: downward fluid with fluid drag force, WOFD: downward fluid without fluid drag force.)

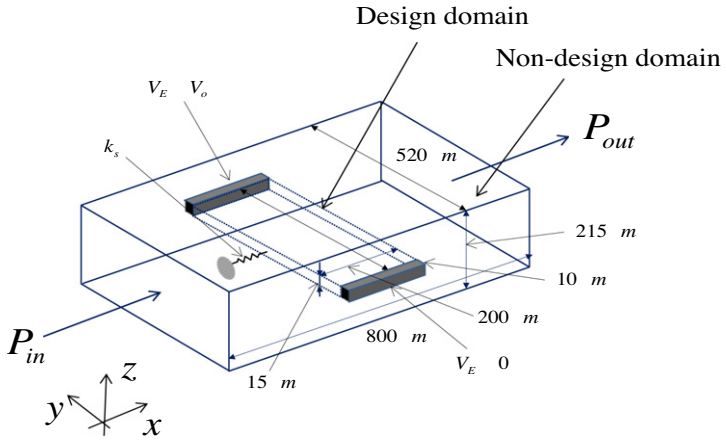

Fig. 11. Synthesis of electro-fluid-thermal-compliant actuator (nickel: k_s = 100 N/m, Young's modulus = 200 GPa, Poisson's ratio = 0.3, depth = 15 μm, electric conductivity = 6.4 $\times 10^6$ K/Ω m, C_{Solid} = 26.07 J/K, thermal conductivity = 90.7 W/km, thermal expansion coefficient = 15 $\times 10^{-6}$ K^{-1}, applied voltage V_0 = 0.3 V, $P_{in} = 10^{-4}$ N/m^2, P_{out} = 0.0 N/m^2, β = 0.4).

where $\delta\mathbf{u}$ is the virtual structural displacement at the piecewise continuous interface boundary. Using the principle of virtual displacements, the following weak form can be derived for the linear elasticity equation for an FSI system

$$\text{Linear elasticity equation}: \quad \int_{ms^t\Omega} \delta\mathbf{S}^{\mathrm{T}}\mathbf{T}_s d\Omega = \int_{s^t\Gamma_i} \delta\mathbf{u}^{\mathrm{T}}(\mathbf{n}\cdot\mathbf{T}_f)d\Gamma. \tag{24}$$

Now, the surface integral of the above equation can be transferred into a volume integration using the divergence theory

$$\int_{s^t\Gamma_i} \delta\mathbf{u}^{\mathrm{T}}(\mathbf{n}\cdot\mathbf{T}_f)d\Gamma = \int_{ms^t\Omega} \nabla_{\mathbf{x}}(\delta\mathbf{u}^{\mathrm{T}}\cdot\mathbf{T}_f)d\Omega. \tag{25}$$

To convert the integral in ${}_{ms}{}^t\Omega$into one in ${}_s{}^t\Omega$, the filtering function (Ψ) for fluid and solid domains is introduced; the function is zero for fluid domains

$$\Psi = \begin{cases} 1 & \text{for solid domain } ({}_{ms}{}^t\Omega) \\ 0 & \text{for fluid domain } ({}_{mf}{}^t\Omega) \end{cases} \tag{26}$$

$$\begin{aligned} \int_{s^t\Gamma_i} \delta\mathbf{u}^{\mathrm{T}}(\mathbf{n}\cdot\mathbf{T}_f)d\Gamma &= \int_{ms^t\Omega} \nabla_{\mathbf{x}}(\delta\mathbf{u}^{\mathrm{T}}\cdot\mathbf{T}_f)d\Gamma \\ &= \int_{s^t\Omega} \Psi\cdot\nabla_{\mathbf{x}}(\delta\mathbf{u}^{\mathrm{T}}\cdot\mathbf{T}_f)d\Omega \end{aligned} \tag{27}$$

By further approximation, the following is obtained:

$$\begin{aligned} \int_{ms^t\Omega} \nabla_{\mathbf{x}}(\delta\mathbf{u}^{\mathrm{T}}\cdot\mathbf{T}_f)d\Gamma &= \int_{s^t\Omega} \Psi\cdot\nabla_{\mathbf{x}}(\delta\mathbf{u}^{\mathrm{T}}\cdot\mathbf{T}_f)d\Omega \\ &= \int_{s^t\Omega} \Psi\delta\mathbf{S}(\mathbf{u},\delta\mathbf{u})^{\mathrm{T}}\mathbf{T}_f + \Psi\delta\mathbf{u}^{\mathrm{T}}\cdot\nabla_{\mathbf{x}}\mathbf{T}_f\, d\Omega \\ &= \int_{s^t\Omega} \left\{-\Psi\delta\mathbf{S}(\mathbf{u},\delta\mathbf{u})^{\mathrm{T}}p - \Psi\delta\mathbf{u}^{\mathrm{T}}\cdot\nabla_{\mathbf{x}}p\right\}d\Omega. \end{aligned} \tag{28}$$

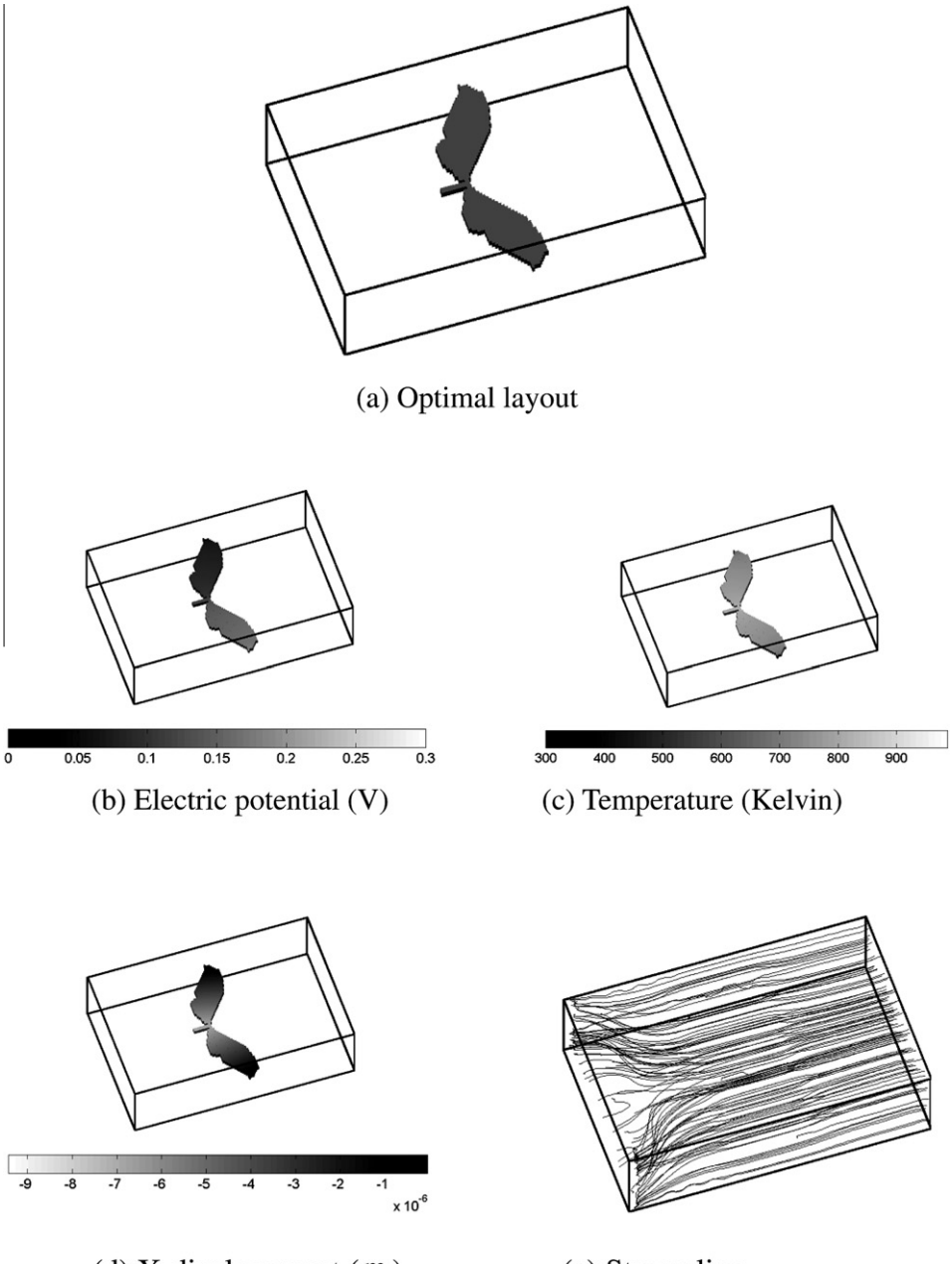

(a) Optimal layout

(b) Electric potential (V)

(c) Temperature (Kelvin)

(d) X-displacement (m)

(e) Streamline

Fig. 12. EFTC actuator design with air (air: electric conductivity = 6.4×10^{-3} K/Ω m, thermal conductivity = 0.025 W/km, C_{Fluid} = 1.012 J/K, density = 1.1839 kg/m^3, viscosity = 17.4 μPa s): (a) optimized layout, (b) electric potential, (c) temperature, (d) x-displacement, and (e) streamline.

It should be noted that (28) is defined in the analysis domain at time t. Therefore, as with the other three physics, we transform the equation into one in the undeformed domain

$$-\underbrace{\int_{s^0\Omega}\delta\mathbf{S}^{\mathrm{T}}\cdot\mathbf{T}_s d\Omega =}_{\text{Geometrically linear analysis}}\int_{s^0\Omega}\Psi\cdot\mathbf{F}^{-\mathrm{T}}\delta\mathbf{S}(\mathbf{u},\delta\mathbf{u})^{\mathrm{T}}\cdot p\|\mathbf{F}\|d\Omega + \int_{s^0\Omega}\Psi\cdot\mathbf{F}^{-\mathrm{T}}\delta\mathbf{u}\cdot\nabla_{\mathbf{x}}p\|\mathbf{F}\|d\Omega. \quad (29)$$

The final equations for the EFTC actuator are summarized in Table 1.

2.2. SIMP interpolation of material properties

To conduct TO of the EFTC devices, the material properties of the four differential equations must be interpolated. The interpolated material properties for each physical parameter are summarized in Table 2. We chose to interpolate the seven material properties in the context of TO. In the electrical equation, the electric conductivity (σ_E) is interpolated from the conductivity of solid ($\sigma_{E,Solid}$) to the conductivity of fluid ($\sigma_{E,Fluid}$). In the fluid equation, only the coefficient of Darcy's force (α) is interpolated from a very large number to zero (a proven concept in [1,5]); the other material properties are set to those of the employed fluid. In the thermal equation, we interpolate the thermal conductivity (σ_T), heat capacity (C_p), and density (ρ) with respect to the design variable, as shown in Eq. (30).

$$\text{Approach 1}: \ (\rho C_p\mathbf{v})\nabla_{\mathbf{x}}T = \begin{cases}(\rho_{Solid}C_{Solid}\mathbf{v})\nabla_{\mathbf{x}}T=\mathbf{0} & \text{for solid or interface boundaries } (\mathbf{v}\equiv\mathbf{0}),\\ (\rho_{Fluid}C_{Fluid}\mathbf{v})\nabla_{\mathbf{x}}T & \text{for fluid},\end{cases} \quad (30)$$

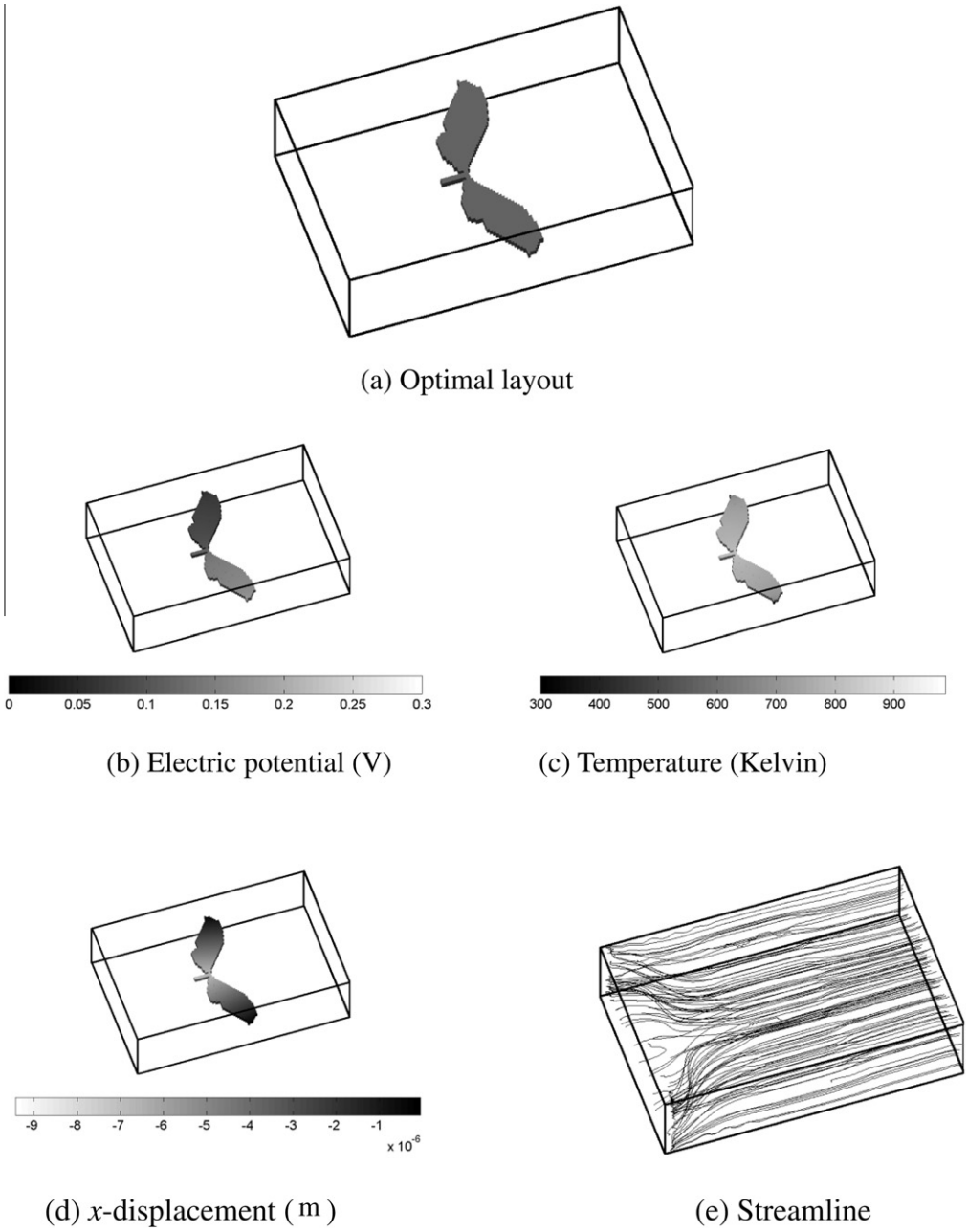

(a) Optimal layout

(b) Electric potential (V)

(c) Temperature (Kelvin)

(d) x-displacement (m)

(e) Streamline

Fig. 13. EFTC design with different thermal interpolations using (31).

Approach 2 : $(\rho C_p \mathbf{v})\nabla_{\mathbf{x}} T$

$$= \begin{cases} (\rho_{Fluid} C_{Fluid} \mathbf{v})\nabla_{\mathbf{x}} T = \mathbf{0} & \text{for solid or interface boundaries } (\mathbf{v} \equiv \mathbf{0}), \\ (\rho_{Fluid} C_{Fluid} \mathbf{v})\nabla_{\mathbf{x}} T & \text{for fluid.} \end{cases} \tag{31}$$

As with the electrical equation, the thermal conductivity (σ_T) is interpolated from that of the solid ($\sigma_{T,Solid}$) to that of the fluid ($\sigma_{T,Fluid}$). In addition, it should be noted that in the first term of the right side of the thermal equation expressed in (7), the density (ρ) and heat capacity (C_p) are multiplied by the fluid velocities ($\mathbf{v}$) and the temperature gradient. Therefore, we may not have to interpolate the heat capacity and density as in Approach 1 and (30). Actually, the term $(\rho C_p \mathbf{v})\nabla_{\mathbf{x}} T$ can be fixed at $(\rho_{Fluid} C_{Fluid} \mathbf{v})\nabla_{\mathbf{x}} T$ as in Approach 2 and (31); this will be demonstrated in the numerical section. We choose to interpolate the density and the heat capacity using Approach 1 and (30).

In the elasticity equation, we interpolate Young's modulus and the fluid stress filter. Young's modulus of the fluid, E_{Fluid}, is much smaller than that of the solid (E_{Solid}). For the interpolation functions, we implement the solid isotropic material with penalization (SIMP) approach with the same penalty value, $n = 3$, for all of the examples ((32)–(38)) in the next section.

Electric conductivity : $\sigma_E(\gamma) = (\sigma_{E,Solid} - \sigma_{E,Fluid})\gamma^n + \sigma_{E,Fluid}$, (32)

Inverse permeability : $\alpha(\gamma) = \alpha_{\max}\gamma^n$, (33)

Thermal conductivity : $\sigma_T(\gamma) = (\sigma_{T,Solid} - \sigma_{T,Fluid})\gamma^n + \sigma_{T,Fluid}$, (34)

Mass density in thermal equation : $\rho(\gamma) = (\rho_{Solid} - \rho_{Fluid})\gamma^n + \rho_{Fluid}$, (35)

Heat capacity : $C_p(\gamma) = (C_{Solid} - C_{Fluid})\gamma^n + C_{Fluid}$, (36)

Young's modulus : $E(\gamma) = (E_{Solid} - E_{Fluid})\gamma^n + E_{Fluid}$, (37)

Fluid stress filter : $\Psi(\gamma) = \gamma^n$, (38)

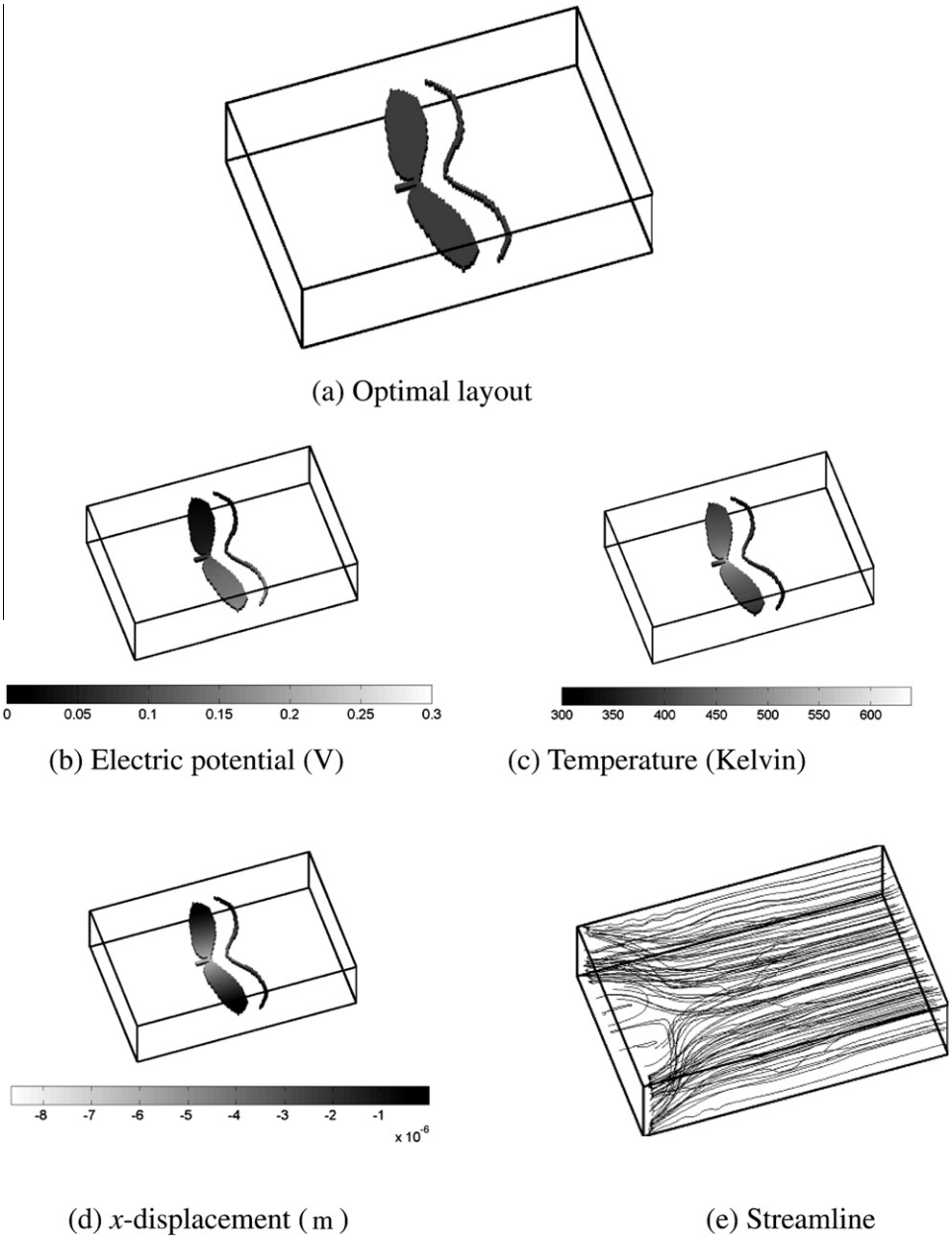

(a) Optimal layout

(b) Electric potential (V)

(c) Temperature (Kelvin)

(d) x-displacement (m)

(e) Streamline

Fig. 14. Design with water (Water: electric conductivity = 6.4×10^{-3} K/Ω m, thermal conductivity = 0.6 W/km, specific heat capacity = 4184 J/K, density = 1000 kg/m^3, viscosity = 1.002 mPa s, $\beta = 0.4$). (a) Optimized layout, (b) electric potential, (c) temperature, (d) x-displacement, and (e) streamline.

where the density design variable defined at each FE is denoted by γ.

2.3. Numerical analysis and sensitivity analysis

To solve the governing equations listed in Table 1, the Newton–Raphson iteration procedure is used. For a simpler discussion, we define the following residual $\Re$ as

$$\Re(\mathbf{V}_E, \mathbf{T}, \mathbf{v}, \mathbf{p}, \mathbf{u}) = \mathbf{0}, \tag{39}$$

where $\mathbf{V}_E$, $\mathbf{T}$, $\mathbf{v}$, $\mathbf{p}$, and $\mathbf{u}$ are the electric potential, temperature, fluid velocities, pressure, and structural displacement vectors in the FE procedure, respectively. To solve the above nonlinear equation, the staggered approach shown in Fig. 5(c) is employed rather than the procedures in Fig. 5(a) and (b). The reason for choosing the staggered approach in Fig. 5(c) is that the interaction between the electric and thermal domains is a one-way coupling, while the interaction between the fluid and structural domains is a mutual coupling. In our numerical tests, the three solution methods yield almost identical solutions. However, one of the advantages of the procedure shown in Fig. 5(c) is that the memory used in the solution procedure is reduced because a tangent stiffness matrix is not built for all of the unknown variables. To calculate the sensitivity value of the objective functions with respect to the design variables, the adjoint variable method (AVM) is used.

2.3.1. Analysis example

To test the present theory, the actuation displacement of the actuator shown in Fig. 6 in air and water is calculated. In water, it can be assumed that the actuator is coated with an insulator such as a SiO substrate to prevent short-circuiting. To embed this microactuator inside of a flow, a larger box with a size of 3000 μm × 1000 μm × 120 μm is modeled. For the fluid boundary condition, a downward flow in the y-direction is assumed at the top boundary of the larger box (Fig. 6). Shown in Fig. 7 are the x- and y-direction displacements, temperature, voltage, equivalent von Mises strain, and streamline when an air flow of 1 μm/s is applied. In Fig. 7(d), the equivalent von Mises strain with an airflow of 1 μm/s is plotted. The developed strain is small enough to assume material linearity in the structural analysis. However, with a higher applied voltage, a local temperature rise where the local stress and associated strain may be higher than the elastic limit is possible. Fig. 8 is a plot of the maximum transverse displacements of point A in Fig. 6 and the maximum temperature in air and water with respect to various fluid velocities; the temperatures with and without fluid drag force are almost identical. When the fluid velocity increases, heat dissipation through conduction and convection and the fluid drag affect the actuator performance. By increasing the fluid velocity, the maximum temperature decreases. Consequently, the structural displacement due to thermal expansion decreases, but the

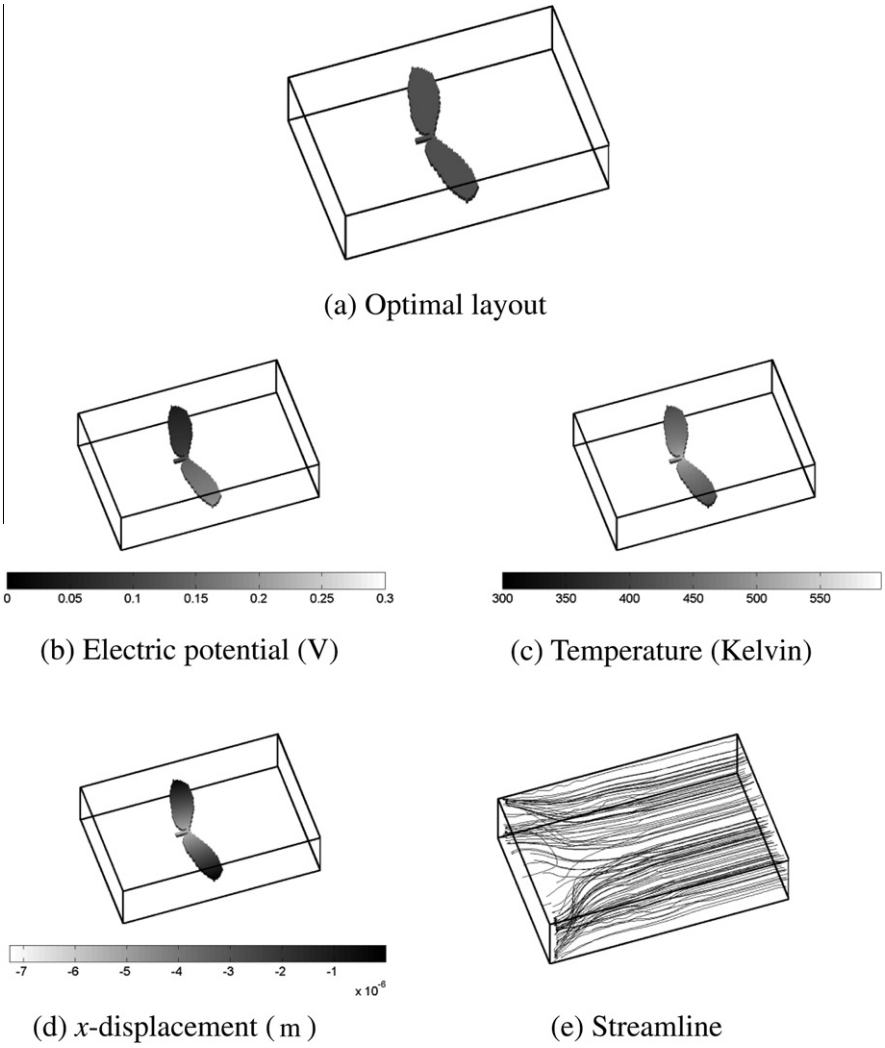

Fig. 15. Reanalysis without the auxiliary heat structure of Fig. 14.

actuator can still move down due to the increased fluid drag with the weak solid structure. This feature can be clearly seen in Fig. 8.

For the second analysis example, a simplified Chevron actuator composed of solids is considered (Fig. 9). As in the first analysis example, the maximum temperature and vertical displacement of point A in Fig. 9(a) were calculated (see Fig. 10) by increasing the downward fluid velocity. As illustrated in Fig. 10, the increase in the air and water fluid velocities serves to lower both the temperature at A as well as overall temperature. Consequently, the displacements also decrease. Because of the low density and heat capacity of air, the vertical displacements and the maximum temperatures with and without considering the fluid drag do not differ. Due to the relatively higher density and heat capacity values for water, significant changes in the values of the displacements are observed. With a faster flow of air and water, the increased heat dissipation lowers the temperature, but the fluid drag force exerted on the actuator pulls down the V-shape actuator.

3. Synthesis of EFTC device

In this section, the application of the developed monolithic formulation and numerical solution method to the TO of an EFTC device is described. For the optimization algorithm, the method of moving asymptotes is employed [34]. In the first design example, we solve the TO problem for a single-direction actuator with two-dimensional (2D) ETC actuator layouts that are available for a possible comparison. The actuator has a relatively simple geometry and boundary condition. It is our belief that such an actuator can serve as a benchmark example because the 2D version of this problem has been widely studied [2,3,6]. In this example, we also test the effects of the type of surrounding fluid and the geometry of the work piece. For the second design example, a programmable actuator that changes its direction depending on the applied voltage is considered so as to demonstrate the versatility of the developed method. In all of the numerical examples presented here, 3D regular meshes are used. The geometry, material properties, and boundary conditions are basically chosen so as to show the potential application of the developed theory. Further validations with more complex and practical systems are currently being investigated.

3.1. Synthesis of single-direction EFTC actuator

Consider a box domain whose size is 800 μm × 520 μm × 215 μm (Fig. 11). Inside this larger box, there is a thin layer with a thickness of 15 μm; this layer is chosen as the design domain (Ω_d). The other domains are filled with fluid. The two sides of this thin layer, which are rendered in gray in the figure, are electrically charged and fixed as solid domains so as to simulate the equal potential condition inside the anode and cathode (perfect conductor). At the front panel of the design domain, a spring with a spring constant of 100 N/m is attached as a substitute for a work piece. To obtain optimal layouts that maximize the stroke of the EFTC actuator to the work piece, the x-displacement (u_A) at the spring is maximized and subject to a mass constraint as follows:

$$\begin{aligned} &\text{Min} \quad u_A \\ &\text{S.t.} \quad \frac{1}{|\Omega_d|}\int_{\Omega_d} \gamma d\Omega - \beta \leqslant 0, \end{aligned} \tag{40}$$

where u_A is the x-direction displacement at the work piece point due to induced thermal expansion, and β and $|\Omega_d|$ are the allowed mass ratio and volume of the design domain, respectively. To

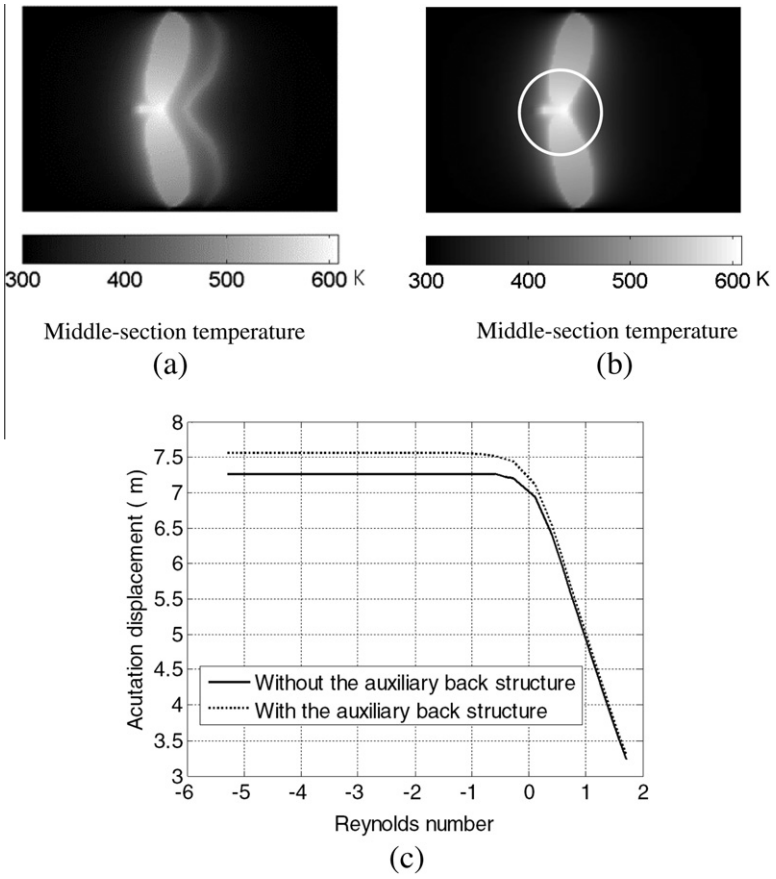

Fig. 16. Comparison of the temperature distribution at the middle sections of the two designs post-processed for intermediate design variables: (a), (b) temperature distributions and (c) the displacements with respect to the Reynolds number (character length = 520 μm).

prevent a complex manifold structure in the z-direction inside the design domain, i.e., a structure with a varying thickness in the z-direction, the design domain (the thin layer) is discretized with one element in the z-direction. The fluid is assumed to flow from the front panel to the back panel due to the input pressure at the front panel; it is possible to use an input velocity profile. It should be noted that the objective in (40) and the simulated boundary condition are similar to the topology layouts of 2D ETC actuators [2,6]. Because of the strong couplings between fluid and thermal domains and between fluid and structural domains, the optimization algorithm should offer optimal layouts so as to maximize the stroke to the spring when considering these strong coupling effects.

The optimized layout when air is selected as the surrounding fluid is shown in Fig. 12(a). As expected, the optimized design is similar to the available designs for ETC actuators. Although not shown here, similar actuation layouts are obtained for slow air velocities because the effects of fluid drag and convection heat dissipation through air are negligible. In addition, some kinks are observed at the two sides due to local optima. Shown in Fig. 12(b)–(e) is the electric potential distribution, temperature distribution, x-direction displacement, and streamline, respectively. The effect of different thermal interpolations using (31) yields a similar result, as shown in Fig. 13. This proves that it is possible to use the alternative interpolation schemes in the temperature equation.

To test the effects of the type of fluid, we change the surrounding fluid from air to water and the design in Fig. 14(a) is obtained. By changing the type of fluid, the significant change in the heat dissipation through conduction and convection is possible. It should be noted that a different mechanism is obtained. As for the design in Fig. 12, the two narrow necks near the mechanical spring experience higher thermal expansions due to the higher Joule energy for actuation. However, an additional narrow structure appears behind the main actuation structure, whose function was not clearly understood. This type of structure has not been obtained before. To clarify the role and effect of this narrow structure, we investigate the temperature distribution at the middle section in Fig. 16(b) and find out that this narrow structure serves as a heater to compensate dissipated energy at the actuation area (marked by a circle in Fig. 16(b)) where most of heat is generated and dissipated. In other words, because of a higher heat capacity and higher conductivity of water when compared to air, the dissipated heat and energy due to the motion of water become significant. Thus, to use the higher conductivity of water to maximize the thermal expansion in the area marked by a circle in Fig. 16(b) and to minimize the heat loss due to the forced convection (which is proportional to the difference between the surrounding fluid temperature and the structure temperature), it seems that this auxiliary structure works as a heater to increase the temperature of the surrounding fluid so as to minimize heat loss due to forced convection. Therefore, it proves that temperature distribution and actuation magnitude are influenced by the type of fluid employed. To examine the effect of the auxiliary structure in more detail, reanalyses with and without this auxiliary structure are performed after post processing for intermediate design variables; the results are shown in Figs. 15 and 16. The maximum displacement decreases from 7.5620 μm to 7.2650 μm and the maximum temperature is also changed from 608.55 K to 597.63 K. It should be noticed that the structure in Fig. 15(a) is similar to the existing actuator structure based on 2D electric-thermal-compliant analysis. In Fig. 15(c), the displacements with various fluid velocities are plotted. As shown in Fig. 16(c), as the fluid velocity is increased, the effect of the auxiliary structure is decreased.

Up to now, in order to simulate a work piece, the spring is simply attached to the design domain without considering its

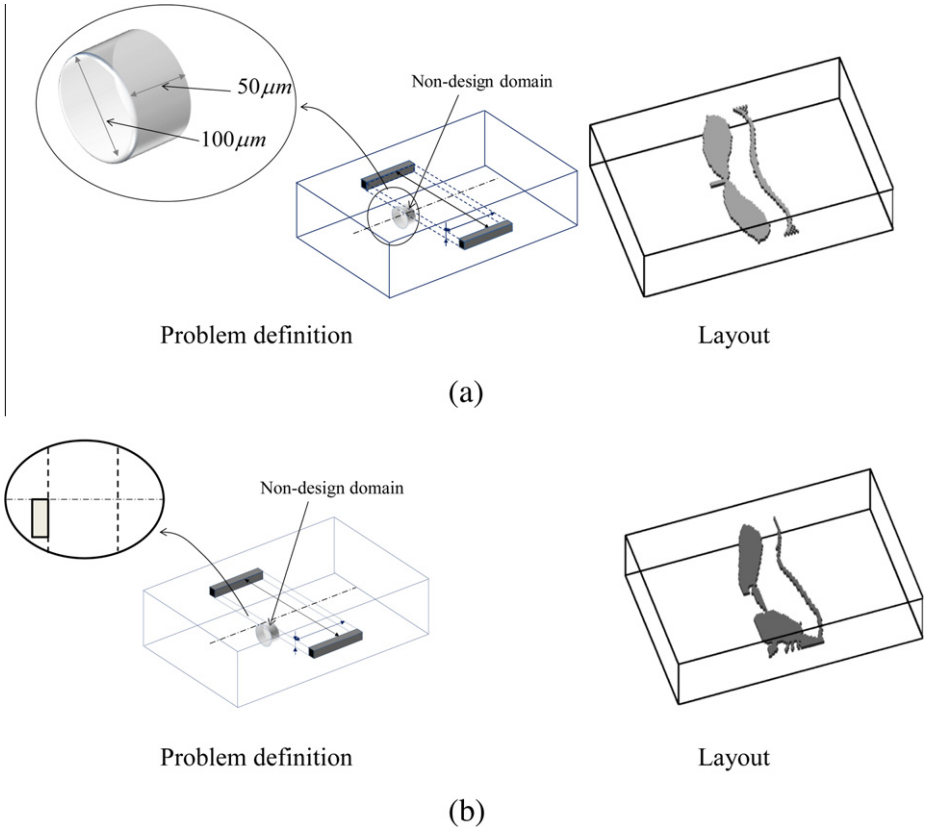

Fig. 17. Test of the work piece geometry with water flow for (a) a centered work piece (tip displacement = 8.2936 μm, max. temperature = 634.1 K); (b) an offset work piece (tip displacement = 6.0316 μm, max. temperature = 653.3 K); and (c) an obstacle (tip displacement = 6.0316 μm, max. temperature = 653.3 K).

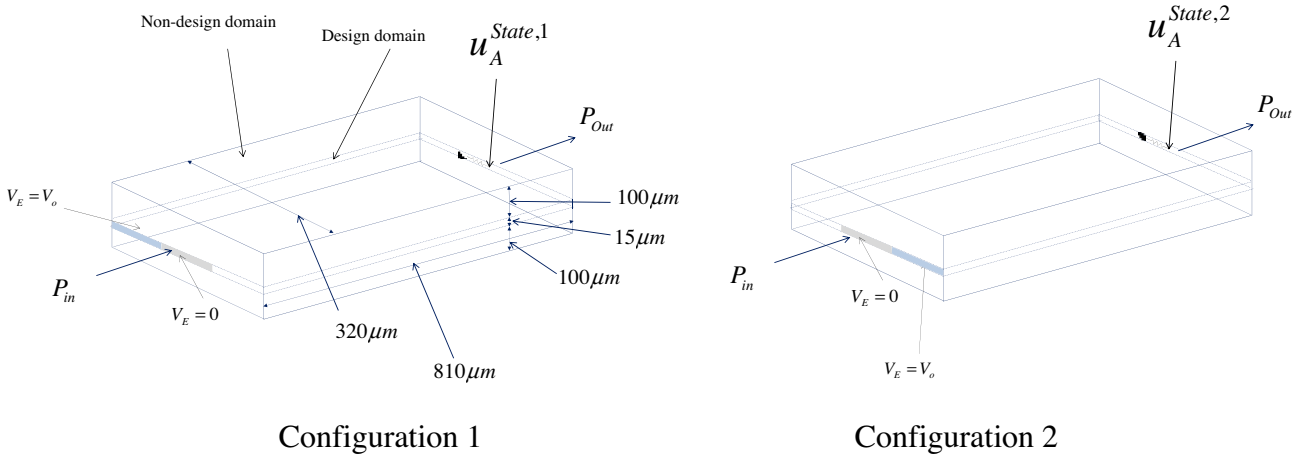

Fig. 18. Synthesis of programmable microactuator (nickel: k_s = 1000 N/m, Young's modulus = 200 GPa, Poisson's ratio = 0.3, depth = 15 μm, electric conductivity = 6.4 × 106 K/Ω m, thermal conductivity = 90.7 W/km, thermal expansion coefficient = 15×10^{-6} K^{-1}, applied voltage V_0 = 0.3 V, $P_{in} = 0.1$ N/m^2, $P_{out} = 0.0$ N/m^2, β = 0.2).

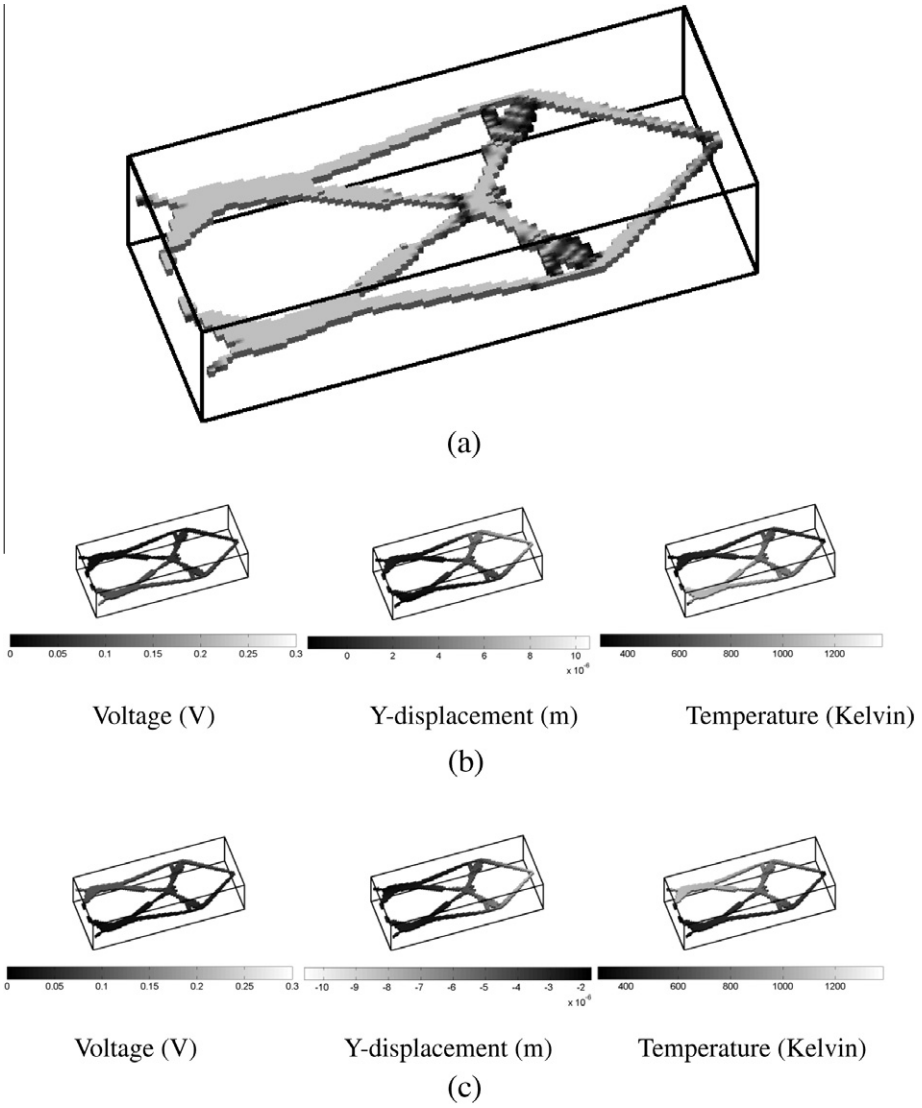

Fig. 19. Optimization results with air (air: electric conductivity = 6.4×10^{-3} K/Ω m, thermal conductivity = 0.025 W/km, specific heat capacity = 1.012 J/K, density = 1.1839 kg/m^3, viscosity = 17.4 μPa s): (a) optimized layout, (b) voltage, y-displacement, and temperature of Configuration 1, and (c) voltage, y-displacement, and temperature of Configuration 2.

geometry. Indeed, it would be interesting to investigate the effect of the work piece geometry on the optimal layout. A cylindrical work piece with a spring constant of $k_s = 100$ N/m is modeled and the optimized layouts shown in Fig. 17(a) and (b) are obtained for two different work piece positions. The advantage of the present numerical method lies in the fact that the simulation is very straightforward without certain simplicities for convection and conduction phenomena or prior tuning.

3.2. Synthesis of programmable microactuator

For the second example, the synthesis of a programmable microactuator shown in Fig. 18 is considered. The goal is to control the actuation direction by changing the applied voltage configurations, which are denoted as Configuration 1 and Configuration 2. Except for the voltage boundary condition, the boundary conditions of Configuration 2, including the fluid boundary condition, are identical to those of the Configuration 1. This type of actuator can be used in microrelays and to manipulate cells. In this example, we want to determine an optimal layout that changes the actuation direction by changing the applied voltage configurations. For the problem, $u_A^{State,1}$ and $u_A^{State,2}$ are used to denote the first and second voltage configurations, respectively

$$\begin{aligned} &\text{Max} \quad u_A^{State,1} - u_A^{State,2} \\ &\text{S.t.} \quad \frac{1}{|\Omega_d|}\int_{\Omega_d} \gamma d\Omega - \beta \leqslant 0. \end{aligned} \tag{41}$$

The obtained optimal layout is shown in Fig. 19. By varying the voltage configurations, we have different actuation directions. Depending on the applied voltage configuration, it is possible to control the actuation direction.

4. Conclusions

After a review of some essential concepts of topology optimization (TO) for an electro-thermal-compliant system, a new TO formulation for an electro-fluid-thermal-compliant (EFTC) system design was presented in the form of a newly developed monolithic solution procedure. The coupling of four physics, i.e., electrical, fluid, thermal, and structure, has never before been attempted for structural optimization. We showed that it is possible to couple these physical parameters in a stable manner using the proposed monolithic modeling approach. For the material and physics interpolations, the seven material properties of these equations were interpolated via the SIMP approach. Compared with previous studies, the heat dissipation due to fluid motion, which leads to forced convection and conduction, and the fluid–structure interaction were newly considered in this study during the optimization process by introducing a modified Navier–Stokes equation and the monolithic concept for FSI. One of the shortcomings of the present formulation is that it requires additional degrees of freedom when compared to the staggered analysis method. However, the proposed formulation makes it possible to conduct TO for an EFTC device. Furthermore, the undershooting problem caused by the constant convection is not observed. Other shortcomings include the assumption of a small displacement in the structural analysis and neglect of the structural displacement effects on the stiffness matrices of the electric potential and temperature. From numerical examples, it was found that consideration of the couplings among electric, fluid, thermal, and structural domains can be important with high heat capacitance and thermal conductivity values. With some fluids having a low conductivity and a low heat capacity, i.e., air, the effects of fluid are small enough and can be neglected. Therefore, it is still valid to use the existing constant convection model.In future studies, the results of the present research can be extended so as to consider the effect of nonlinear material properties and to design more complex MEMS devices. Furthermore, in future research it will be important to consider the effect of large displacements in calculating the stiffness matrices of an EFTC system.

Acknowledgement

This research was supported by Basic Science Research Program through the National Research Foundation of Korea (NRF) funded by the Ministry of Education, Science and Technology (2011-0027359).

References

[1] G.H. Yoon, Topology optimization for stationary fluid–structure interaction problems using a new monolithic formulation, Int. J. Numer. Methods Engrg. 82 (2010) 591–616.
[2] S. Heo, G.H. Yoon, Y.Y. Kim, Minimum scale controlled topology optimization and experimental test of a micro thermal actuator, Sensor Actuator A 141 (2008) 603–609.
[3] M.P. Bendsøe, O. Sigmund, aTopology Optimization Theory, Methods and Applications, Springer-Verlag, New York, 2003.
[4] G.H. Yoon, O. Sigmund, A monolithic approach for electrostatic problems, Comput. Methods Appl. Mech. Engrg. 197 (2008) 4062–4075.
[5] T. Borrvall, J. Petersson, Topology optimization of fluids in Stokes flow, Int. J. Numer. Methods Fluids 41 (2003) 77–107.
[6] O. Sigmund, Design of multiphysics actuators using topology optimization – Part I: One material structure, Comput. Methods Appl. Mech. Engrg. 190 (2001) 6577–6604.
[7] L. Yin, G.K. Ananthasuresh, A novel topology design scheme for the multiphysics problems of electro-thermally actuated compliant micromechanisms, Sensor Actuator A 97–98 (2002) 599–609.
[8] J.S. Choi, J.H. Yoo, Structural optimization of ferromagnetic materials based on the magnetic reluctivity for magnetic field problems, Comput. Methods Appl. Mech. Engrg. 197 (49–50) (2008) 4193–4206.
[9] Y.D. Seo, H.J. Kim, S.K. Youn, Shape optimization and its extension to topological design based on isogeometric analysis, Int. J. Solids Struct. 47 (2010) 1618–1640.
[10] E. Lemaire, V. Rochus, J.C. Golinval, P. Duysinx, Microbeam pull-in voltage topology optimization including material deposition constraint, Comput. Methods Appl. Mech. Engrg. 197 (45–48) (2008) 4040–4050.
[11] S. Nishiwaki, T. Nomura, S. Kinoshita, K. Izui, M. Yoshimura, K. Sato, K. Hirayama, Topology optimization for cross-section designs of electromagnetic waveguides targeting guiding characteristics, Finite Elem. Anal. Des. 45 (12) (2009) 944–957.
[12] W.M. Rubio, S. Nishiwaki, E.C.N. Silva, Design of compliant mechanisms considering thermal effect compensation and topology optimization, Finite Elem. Anal. Des. 46 (12) (2010) 1049–1060.
[13] Y.S. Yang, Y.H. Lin, Y.C. Hu, C.H. Liu, A large-displacement thermal actuator designed for MEMS pitch-tunable grating, J. Micromech. Microeng. 19 (2009) 1–23.
[14] T. Moulton, G.K. Ananthasuresh, Micromechanical devices with embedded electro-thermal-compliant actuation, Sensor Actuator A 90 (2001) 38–48.
[15] L. Chang, Foundations of MEMS, PEARSON, 2005.
[16] W. Weison, T.L. Svetlana, B.L. Walter, V. Richard, Design of a bidirectional MEMS actuator with high displacement resolution large driving force and power-free latching, Microelectron. Engrg. 85 (2008) 587–598.
[17] A. Iga, S. Nishiwaki, K. Izui, M. Yoshimura, Topology optimization for thermal conductors considering design-dependent effects including heat conduction and convection, Int. J. Heat Mass Transfer 52 (11–12) (2009) 2721–2732.
[18] O. Sardan, D.H. Petersen, K. Mølhave, O. Sigmund, P. Bøggild, Topology optimized electrothermal polysilicon microgrippers, Microelectron. Engrg. 85 (5–6) (2008) 1096–1099.
[19] H.N. Kwon, S.H. Jeong, S.K. Lee, J.H. Lee, Design and characterization of a micromachined inchworm motor with thermo elastic linkage actuators, Sensor Actuator A 103 (2003) 143–149.
[20] L. Que, J.S. Park, Y.B. Gianchandani, Bent-beam electrothermal actuators—Part I: Single beam and cascaded devices, J. Microelectromech. Syst. 10 (2) (2001) 247–254.
[21] V. Jorge, T.T. Margarita, H.A. Anas, Design of MEMS vertical–horizontal chevron thermal actuators, Sensor Actuator A 153 (1) (2009) 127–130.
[22] H.Y. Chan, W.J. Li, Design and fabrication of a micro thermal actuator for cellular grasping, Acta Mech. Sin. 20 (2) (2004) 132–139.
[23] N. Chronis, L.P. Lee, Electrothermally Activated SU-8 Microgripper for Single Cell Manipulation in Solution, J. Microelectromech. Syst. 14 (4) (2005) 857–863.
[24] W.C. Chang, D.W. Sretavan, Microtechnology in medicine: the emergence of surgical microdevices, Clin. Neurosurg. (54) (2007) 137–147.

[25] W. Zhang, M. Gnerlich, J.J. Paly, Y. Sun, G. Jing, A. Voloshin, S.T. Lucic, A polymer V-shaped electrothermal actuator array for biological applications, J. Micromech. Microeng. 18 (2009) 1–8.
[26] L. Lin, J. Jones, A Liquid-filled buoyancy-driven convective micromachined accelerometer, J. Microelectromech. Syst. 14 (5) (2005) 1061–1069.
[27] N.T. Nguyen, D. Bochnia, R. Kiehnscherf, W. Dotzel, Investigation of forced convection in microfluid systems, Sensor Actuator 55 (1996) 49–55.
[28] B.C. Kaanta, H. Chen, X. Zhang, Effect of forced convection on thermal distribution in micro thermal conductivity detectors, J. Micromech. Microeng. (2011), doi:10.1088/0960-1317/21/4/045017.
[29] R.V. Loon, P.D. Anderson, F.N.V.D. Vosse, S.J. Sherwin, Comparison of various fluid–structure interaction methods for deformable bodies, Comput. Struct. 85 (2007) 833–843.
[30] K.C. Park, C.A. Felippa, R. Ohayon, Partitioned formulation of internal fluid–structure interaction problems by localized lagrange multipliers, Comput. Methods Appl. Mech. Engrg. 190 (2001) 2989–3007.
[31] G.H. Yoon, Topological design of heat dissipating structure with forced convective heat transfer, J. Mech. Sci. Technol. 24 (6) (2010) 1225–1233.
[32] K.J. Bathe, Finite Element Procedures, Prentice hall, New Jersey, 1996.
[33] W.P. Sassena, V.A. Hennekena, M. Tichema, P.M. Sarrob, Contoured thermal V-beam actuator with improved temperature uniformity, Sensor Actuator A 144 (2008) 341–347.
[34] K. Svanberg, The method of moving asymptotes – a new method for structural optimization, Int. J. Numer. Methods Engrg. 24 (1987) 359–373.